Extreme vertical drafts in the polar summer mesosphere: A mesospheric super bore?

J. L. Chau[1], R. Marino[2], F. Feraco[2,3], J. M. Urco[1,4], G. Baumgarten[1], F.-J. Lübken[1], W. K. Hocking[5], C. Schult[1], T. Renkwitz[1], R. Latteck[1]

[1]Leibniz-Institute of Atmospheric Physics at the University of Rostock, Kühlungsborn, Germany
[2]Laboratoire de Mécanique des Fluides et d'Acoustique, CNRS, École Centrale de Lyon, Université Claude Bernard Lyon 1, INSA de Lyon, Écully, France
[3]Dipartimento di Fisica, Universitá della Calabria - Arcavacata di Rende (CS), Italy
[4]Department of Electrical and Computer Engineering and Coordinated Science Laboratory, University of Illinois Urbana-Champaign, Urbana, IL, USA
[5]Department of Physics and Astronomy, University of Western Ontario, London, Ontario, Canada

Key Points:

- First observations of extreme vertical velocities in the mesosphere. They might result from the interplay of gravity waves and turbulence.
- The observed spatio-temporal structures resemble a mesospheric bore, with large vertical extent and vertical velocities (a Super Bore).
- Such extreme events might have been missed or ignored in previous observations of vertical velocities or other mesospheric parameters.

Corresponding author: Jorge L. Chau, chau@iap-kborn.de

Abstract

The polar summer mesosphere is the Earth's coldest region, allowing the formation of mesospheric ice clouds. These clouds produce strong polar mesospheric summer echoes (PMSE) that are used as tracers of mesospheric dynamics. Here we report the first observations of extreme vertical drafts (± 50 ms^{-1}) in the mesosphere obtained from PMSE, characterized by velocities more than five standard deviations larger than the observed vertical wind variability. Using aperture synthesis radar imaging, the observed PMSE morphology resembles mesospheric bores, i.e., narrow along propagation (3–4 km) and elongated ($>$ 10 km) transverse to propagation direction. Additionally, our event presents a large vertical extent ($\pm$ 3–4 km), resembling a "super bore". Powerful vertical drafts, intermittent in space and time, emerge also in direct numerical simulations of stratified flows, predicting non-Gaussian statistics of vertical velocities. This evidence suggests that our event, and perhaps previous bores, might result from the interplay of gravity waves and turbulent motions.

Plain Language Summary

Extreme events are ubiquitous of geophysical flows. Example of these events are tornadoes and Rogue waves in the lower atmosphere and oceans, respectively. In the mesosphere, the boundary of Earth's atmosphere and outer space, extreme events could also occur, although this region is poorly observed. Here we present the first observations of vertical velocities more than five times their expected standard deviation. These observations are possible by tracking and imaging strong mesospheric radar echoes that occur in the summer at polar latitudes, with a radar used in a radio camera mode. The morphology of our observations resembles previously observed instabilities called bores or wave walls, but with much larger vertical velocities and vertical extents. Direct numerical simulations of stratified flows predict the occurrence of these extreme vertical velocities.

1 Introduction

Extreme events are ubiquitous to geophysical flows, e.g., tornadoes or rogue waves (e.g., Tippett & Cohen, 2016; Adcock & Taylor, 2014). In the mesosphere (60–90 km), extreme events could also exist. This region is difficult to observe since it is too high for meteorological balloons, and too low for satellites to fly in and make in-situ measurements. Therefore, observations of extreme events and their respective impacts in this region are not easy to identify and study. Nonetheless, this atmospheric region hosts a number of interesting optical and radio phenomena like noctilucent clouds (NLC) and polar mesospheric summer echoes (PMSE) (e.g., Thomas & Olivero, 1986; Ecklund & Balsley, 1981; Hoppe et al., 1988).

During summer months at mid and high latitudes, the mesosphere is the coldest place on Earth with temperatures as low as 130 K due to dynamical processes that drive the atmosphere away from radiatively controlled state (e.g., Lübken et al., 1999). One of the most challenging, important, and intriguing mesospheric measurements are vertical winds. Vertical winds are usually smaller than horizontal winds, but they have significant effects on the atmospheric dynamics, composition, and electrodynamics (e.g., Larsen & Meriwether, 2012). Their mean synoptic-scale values are expected to be in the order of centimeters per second and are difficult to measure directly (e.g., Gudadze et al., 2019). On the other hand measurements made with ground-based radars, passive optics, lidars, as well as in-situ chemical traces, show high values varying by up to ± 10 ms^{-1} (e.g., Hoppe & Fritts, 1995; Gardner & Liu, 2007; Lehmacher et al., 2011). Similar and even higher values have been observed at higher altitudes in the thermosphere (e.g., Larsen & Meriwether, 2012). These high values can occur with the same sign for minutes to hours.

Although part of this variability is attributed to Kelvin-Helmholtz and other instabilities (e.g., Chau et al., 2020), the drivers for the majority of observations of large and/or persistent values are not obvious. Waves propagating through the region appear to be connected to the vertical wind variability; either they come from below or are generated locally via instabilities, nonlinear interaction with other waves or turbulence (e.g., Gardner et al., 1995; Fritts et al., 2004; Larsen & Meriwether, 2012). Moreover, high variability in vertical winds have been reproduced in direct numerical simulations (DNS) in flows similar to those in the mesosphere (Marino et al., 2015), including extreme values under some special flow conditions (Feraco et al., 2018). Understanding and character-

izing the vertical wind variability of the mesosphere and higher altitudes (thermosphere) are important for explaining their effects on dynamics, composition, chemistry, and electrodynamics of these regions (e.g., Larsen & Meriwether, 2012), and perhaps their possible connection to biological-size particles rising up from the troposphere into near space (Berera & Brener, 2020).

In this work, we focus on extreme vertical drafts observed in the polar summer mesosphere. These observations have been made with the Middle Atmosphere Alomar Radar System (MAARSY) located in northern Norway (69.30°N, 16.04°E). Observations of PMSE have been routinely made with MAARSY since 2010 (Latteck et al., 2012). After more than 20 years of active research, the physics behind PMSE is well understood. Their signal strength depends on electron density, turbulence, and charged-ice particles (e.g., Rapp & Lübken, 2004) and they are good tracers of atmospheric winds (e.g., Sato et al., 2017).

Based on two summers of continuous observations and many years of experience, the event we present is extreme since our measured vertical velocities reach high values more than five times their standard deviation (σ_w). We start describing the observing modes followed by a description of the modeling employed in this work. Our radar and DNS results are presented in Section 4, followed by a discussion and possible connections to previously observed mesospheric bores.

2 Radar observing modes

MAARSY is an active phased array that consists of 433 three-element cross-polarized Yagi antennas and operates at 53.5 MHz. Its main beam one-way half-power beam-width is 4°. On reception, either all 433 elements, or up to 7 groups of 49 elements, or up to 15 out of 55 groups of 7 elements can be used (e.g., Latteck et al., 2012, for more details).

PMSE are routinely observed with MAARSY using two quasi-simultaneous main modes: (a) multi-beam, and (b) radar imaging (e.g., Gudadze et al., 2019; Urco et al., 2019). These modes have been used during the summers of 2016 and 2017, except for a few days where other modes were used to support special requests. Both modes run with 1 ms interpulse period. Since horizontal winds are expected to be within ± 150 ms^{-1}, the multi-beam mode has been configured to allow a Nyquist velocity of ± 35 ms^{-1}. On the other hand the radar imaging mode allows a Nyquist velocity of ± 175 ms^{-1}, suitable to study other echoes, e.g., non-specular meteor echoes (Chau et al., 2014).

Given the velocity aliasing in the multi-beam mode, in this work we use only data from the radar imaging mode, which observes for 30 s every 180 s. This mode uses only one vertically pointing transmitting beam using all 433 elements, while 16 antenna groups are used on reception, 15 of them for radar imaging. A spectral moment method has been implemented to obtain: signal, mean radial velocity and spectral width. Radial velocities from slightly off-vertical locations could have contributions from horizontal velocities. However, unrealistic supersonic horizontal winds (more than 1500 ms^{-1}) would be required to generate the large (~ 50 ms^{-1}) observed velocities.

Radar imaging has been obtained by applying the Maximum Entropy method on the cross-spectra data from combinations of receiving antenna pairs (e.g., Hysell & Chau, 2006; Urco et al., 2019). Since the selected 15 receiving antennas do not have the same beam width, the imaging inversion has been performed only within $\pm 8^\circ$ zenith angles. This angular coverage also allows for the observation of PMSE outside the main illuminated area, if strong echoes are present there.

3 Direct numerical simulations of extreme events

In many cases the atmosphere can be considered as being nearly incompressible, allowing for the investigation of its dynamics by means of DNS of the Navier-Stokes equations in the Boussinesq approximation. In this framework, the parameter governing the stratification is the so-called Froude Number, defined as $\mathrm{Fr} = UL/N$ (N = Brunt-Väisälä frequency, while L and U are the characteristic length and velocity, respectively), which provides a measure of the relative strength of gravity waves against non-linearities. The turbulence strength is provided by the classical Reynolds number, $\mathrm{Re} = UL/\nu$, where ν is the kinematic viscosity. Another important parameter is the Buoyancy Reynolds number $\mathrm{Rb} = \mathrm{ReFr}^2$, that helps to identify regimes where either waves dominate the dynamics or turbulence has to compete with gravity waves in transferring the energy across the scales (e.g., Pouquet et al., 2018).

The DNS presented in this study was produced by integrating the Boussinesq equations in the case of stable stratification assuming incompressibility. The equations are implemented in their non-dimensional form and temporal evolution is obtained with a second-order Runge-Kutta scheme. The simulations were forced with a random isotropic mechanical forcing $\mathbf{F}$ (Marino et al., 2014). The runs have been initialized ($t = 0$) with

a random velocity field and zero potential temperature gradients. The Geophysical High-Order Suite for Turbulence code is used to integrate the equations numerically. The Boussinesq equations are solved numerically without using any parametrization of the smaller scales on an isotropic grids of 512^3 points for up to 400τ eddy turnover times, where $\tau = U/L$ (e.g., Feraco et al., 2018, for more details).

4 Results

4.1 Radar Observations

The extreme event of vertical drafts that occur on July 16, 2016 is shown in Figures 1a to 1c. Figure 1a shows the signal-to-noise ratio (SNR) as a function of altitude and time. The mean vertical velocity and spectral width are shown in Figures 1b and 1c, respectively.

The event in question occurred between 04:25 and 05:00 universal time (UT) and is characterized by: (a) episodes of large vertical updrafts and downdrafts lasting a few minutes at around 86 km, (b) large spectral widths, and (c) echoes appearing to move up and down according to the measured mean vertical velocities, and (d) their strength increasing (decreasing) when going up (down). Outside this time interval, the PMSE spectral moments behave within expected values, i.e., vertical velocities within ± 5 ms^{-1}, spectral widths below 5 ms^{-1}, and echoes occurring in multiple layers.

In Figures 1d to 1t normalized spectrograms for selected times around the extreme event are shown. Each spectrum is obtained from $\sim$30 s continuous observations. The striking features in this figure are the large positive and negative vertical drafts well outside $3\sigma_w$, reaching high absolute values (e.g., 65 ms^{-1} at 04:28:21 UT or -45 ms^{-1} at 04:36:03 UT). Except for the spectra at 04:41:11 (1o) and 04:43:46 (1n) UT, the spectra are composed of one or two velocity peaks at a given altitude. Given that the illuminated volume has a radius of about $\sim$ 5 km in the horizontal direction at these altitudes , the multi peak features are a result of multiple regions of enhanced backscattering within the illuminated volume. The presence of multiple peaks gives rise to large values of spectral widths. The red dashed lines indicate the $3\sigma_w$ based on two months of continuous observations in 2016.

From radar imaging, we have obtained spatial information of features within the illuminated volume. Figures 2a to 2f show selected 2D spatial planes of imaging around

04:30:54 UT. The large scale 30-min averaged horizontal winds obtained from a closely located specular meteor radar are shown in arrows as a reference. Radar imaging results clearly indicate that the extreme updrafts and downdrafts are localized in horizontal space, with 3–4 km width along the x axis, and at least 8–12 km elongation along the y axis, where x- and y-axis are rotated 50° East of North. An animation of similar frames from 04:00 to 05:30 UT every 150–170 s can be seen in Movie S1. The imaging results are also used to verify that the inferred vertical velocities are mainly due to vertical wind and not to a horizontal wind contamination, since areas of large vertical drafts are observed at or close to overhead inside the vertical transmitting beam. For typical mesospheric horizontal winds ($\pm$150 ms^{-1}), their contamination in our vertical estimates would be at most 5–8 ms^{-1}.

The temporal evolution of these spatial features is summarized in Figures 2g to 2n as function of x (i.e., X-Time Doppler-Intensity, XTDI) (left) and y (YTDI) (right) for selected altitudes. The extreme drafts are elongated along y at all altitudes, and drift along x. At 89 km, the updraft is observed to cover at least 16–20 km in x, appearing around 04:20 and disappearing around 04:45 UT. The irregularities causing these echoes move up from around 86 km and stay at 89 km for at least 25 min. At 81.5 km, downdrafts are also elongated along the y axis and drift generally along x. However, they are only observed for 2–4 km along x and last less than 5 min. The latter suggests that the irregularities came down from 86 km or so and disappear after a few minutes. Later the echoes appear again around 04:55 due to irregularities coming from below and remain present at least until 05:30 UT. Both regions of updrafts and downdrafts drift at $\sim$11 ms^{-1} along x, North-East, with respect to an observer on the ground. Note that regions of large drafts are observed for a longer time in these plots than in the spectra plots in Figure 1, since the spectra were obtained using all 433 elements on transmission and reception. The duration, elongation and horizontal extent of the event should be taken as minimum values, given the relatively small observing volume, when compared to other imaging observations (e.g., airglow imagers).

Mean horizontal winds representing an area of approximately 400 km diameter at 86 km obtained with a collocated specular meteor radar system show that a moderate horizontal wind shear (24 ms^{-1}km^{-1}), occurs at the altitude where the extreme updrafts and downdrafts begin, i.e., 86 km (see Figure S1).

4.2 DNS results

DNS results presented here are obtained with $Fr \simeq 0.076$, $Rb \simeq 22$ and with $Re \sim 4000$, the latter being smaller than but not too far from Re estimated in the MLT (e.g., Fritts et al., 2014; Chau et al., 2020). Based on Feraco et al. (2018), these parameters correspond to the peak of the resonant regime identified in terms of Fr (and Rb) where extreme events in both the velocity and the temperature field have the chance to develop (see e.g., Feraco et al., 2018, Figure 5) .

The resulting PDF of w, computed over an extended time interval ($46\tau < t < 406\tau$, beyond the peak of the dissipation achieved by this DNS flow), is characterized by a kurtosis $K_w = 6.6$ (see Figure S2). This value is much larger than the Gaussian reference ($K_w = 3$). By integrating the tails of the PDF, the probability of observing grid values of w larger than $5.5\sigma_w$ is $\sim 0.1\%$ for the present study.

Figures 3a and 3b show two-dimensional renderings of w (in units of the standard deviation $\hat{w} = w/\sigma_w$) at a selected time for yx and yz cuts, respectively. These renderings exhibit at times a morphology similar to that of the mesospheric bores on ducting regions. Indeed, in Figure 3a it is possible to appreciate finger-like structures or patches of the flow in a horizontal plane corresponding to strong updrafts and downdrafts, resembling our MLT observations. The coherence of these structures is lost in fractions of a turnover time of the simulation (see Movie S2). Figure 3b is instead a vertical yz-cut of the same DNS output (at $t = 311.22\tau$), showing the alternation of updrafts and downdrafts which sometimes appear in pairs. Figure 3c shows the vertical profile of the horizontal wind shear $|\mathbf{S}| =< dv_\perp/dz >_h$ (where the average is performed over horizontal planes and $v_\perp$ is the horizontal wind) together with the number of grid points by-plane where $w > 5.5\sigma_w$. The structures visible in Figures 3a and 3b, at a given time, are made of many grid points above the $5.5\sigma_w$ threshold. This definition of "extreme event" in the numerical study is slightly different than in our observations, where we refer to "extreme event" as to the observation in the MLT of a localized structure with high vertical velocity, extensive in space and time.

The probability to observe the extreme events in w conditioned to the values of horizontal wind shear is shown in Figure 3d. The joint statistics shows clearly that the probability of observing extreme vertical drafts is very close to zero in planes where the horizontal wind shear is vanishing or very small ($|\hat{\mathbf{S}}| < 0.35$, where $\hat{\mathbf{S}} = \mathbf{S}/\sigma_S$ and σ_S is

the standard deviation of $|\mathbf{S}|$). Moreover, the cumulative probability of observing any extreme values of w (indicated with the dashed line) is smaller than the 1% for $\hat{\mathbf{S}} < 0.5$, which means that moderate to strong horizontal wind shears are a necessary (though not sufficient) condition in order to observe extreme vertical drafts. The joint PDF also shows that the probability of observing the most powerful drafts ($> 13\sigma_w$) saturates very quickly, again at around $\hat{\mathbf{S}} \sim 0.8$, and remains constant. Since our observed PMSE event is associated with a moderate horizontal wind shear, we can therefore speculate that the wave-turbulence resonant mechanism responsible for the outcome of the present numerical study might indeed be involved in the production of the extreme MLT vertical velocities reported here.

5 Discussion and Conclusions

5.1 Connection to mesospheric bores

A sketch based on the observations is shown in Figure 4. The SNR, vertical velocity, and spectral width from Figure 1 are combined into an altitude-time-Doppler intensity plot (e.g., Chau et al., 2020), with superimposed maximum w values and expected regions of horizontal wind convergence (C) and divergence (D). Based on Figure 1i, the estimated local horizontal wind convergence is $\sim$14 $\mathrm{ms}^{-1}\mathrm{km}^{-1}$ assuming an incompressible flow, which is more than 100 times the measured mesoscale horizontal divergence in this region (Chau et al., 2017). This sketch together with the spatial features shown in Figure 2 resembles the undular mesospheric bore features of Bore 1 reported by Fritts et al. (2020), where they combined 2D images of PMC and lidar vertical profiling. As in the case of Fritts et al. (2020), we also expect that the observed vertical velocity divergence (convergence) ahead of (behind) the extreme event is accompanied by horizontal wind convergence (divergence). This horizontal wind behavior, unfortunately, could not be directly measured in our case. Note that the large local horizontal wind convergence/divergence is expected at the central altitude and not where the high vertical velocities are observed.

The vertical dimensions of our event are more than two times larger than those reported by Fritts et al. (2020), i.e., $2h_1 \sim 12$ and $2h_0 \sim 4.5$ km, instead of 4.7 and 2.8 km, respectively, where $2h_1$ and $2h_0$ are the vertical extensions during the peak of the perturbation and outside the perturbation. These dimensions imply a normalized bore am-

plitude $\beta = (h_1 - h_0)/h_0 \sim 1.67$ which is much larger than previously measured or inferred characteristics of mesospheric bores or wall waves (e.g., Taylor et al., 1995; Li et al., 2007; Smith et al., 2017). Vertical velocities in previous mesospheric bores have been expected or measured to be less than 10 ms^{-1} (e.g., Li et al., 2007).

Morphologically our extreme event resembles a mesospheric bore, but given its vertical dimensions and observed vertical velocities, we call it a Super Bore! We are not able to fully identify all details of the flow fields and causes of the observed extreme event. Based on DNS results the observed super bore, and possibly other mesospheric bores, might be due to a resonant interaction between gravity waves and turbulent motions in stratified flows with Fr $\sim 0.1 - 0.01$. Not only the DNS results produce extreme w events, but these events appear in finger-like patches in the horizontal plane localized in vertical channels (ducts) with moderate horizontal wind shears, i.e., showing features of previous bore theories (e.g., Dewan & Picard, 2001; Laughman et al., 2009). Further observations as well as theory and modelling efforts are still needed to find and identify the specific sources of mesospheric bores, including super bores.

5.2 How often mesospheric extreme events occur?

We have presented only one extreme event, however, the DNS results suggest that such events should occur more often than expected from traditionally assumed Gaussian distributed w, i.e., 1 in one thousand instead of 1 in 3 million for a given Froude number in the range Fr $\sim 10^{-2} - 10^{-1}$. Why have they not been observed before?

In the case of previous PMSE observations with MAARSY, the great majority were done with Nyquist velocities less than 30 ms^{-1}. Therefore, extreme drafts have been filtered out and cannot be recovered by their velocity values. In cases where larger Nyquist velocity have been used, they were presumably treated as outliers given their large values and relative short duration (e.g. Gudadze et al., 2019, Figure 4). In the latter cases, a careful reprocessing should be pursued to search for additional extreme drafts.

Such extreme drafts are not expected to be unique to the polar summer mesosphere. Based on DNS the main ingredients are moderate-strong stratification (Fr $\sim 10^{-2} - 10^{-1}$) and moderate horizontal wind shears. Thus, one should search for extreme vertical velocities at other latitudes, seasons, altitudes, with a variety of instruments. For example, mesospheric solitary waves (solitons) reported from foil chaff experiments in

the past, might have sampled a small spatial and temporal portion of an extreme event like the one reported here (Widdel, 1991).

Although our work is focused on vertical velocities, such extreme events should show up in other atmospheric variables, e.g., temperatures, airglow intensities, NLC brightness, etc. As far as we know, extreme events based on these parameters have not been reported so far, or they might have been ignored.

5.3 Potential impacts

In the particular case of the polar summer mesosphere, ice particles exist and they are the main reason for the presence of NLC and PMSE (e.g. Thomas & Olivero, 1986; Rapp & Lübken, 2004). Using expected temperature and pressure profiles from empirical models as well as the observed vertical drafts, we find that in our specific case the temperature increases significantly in the downdraft regions. This increase causes the reduction of ice particle radius in time scales of a few minutes (see Figure S3). In the case of PMSE, their volume reflectivity is mainly determined by the Schmidt number, which is proportional to the square of ice particle radius (e.g., Rapp & Lübken, 2004). Therefore a reduction of ice particle radius would mean a weaker PMSE. In Figure 1a, the strength of echoes decreases or echoes even disappear for the regions experiencing downdrafts. In the updraft regions, the strength of echoes increases but based on our calculations this increase is not related to the ice particle radius, instead it could be due to an increase of electron density. These simple calculations indicate that indeed ice particle radius is affected by extreme vertical drafts, and so are clouds and echoes relaying on it.

Like in the case of ice particles, other mesospheric species would also experience significant changes in altitude, and therefore their mixing ratios might change at a given altitude. The transport of photochemically inactive species across the turbopause by vertical winds enhances their concentration much more rapidly compared to turbulent mixing, which implies that extreme vertical updrafts are an effective mechanism to transport trace gases into the lower thermosphere. For example if Argon and molecular Nitrogen are brought to higher altitudes, e.g., from 90 to 110 km, it could take up to 3 h to fully mix these components, i.e., much longer than if these species would have stayed at 90 km (e.g., Von Zahn et al., 1990).

Our current poor knowledge on these extreme drafts (formation, occurrence rate, duration, predictability) as well as limited observing capabilities in the mesosphere, should not impede the exploration of impacts on other fields where km-scale perturbations and instabilities and high vertical drafts might be important. For example, if they occur frequently a better understanding and characterization would contribute to the roles of such dynamics (including short-scale gravity waves and instability dynamics) in a number of parameters that require parameterization in large-scale general circulation weather and climate models (e.g., Fritts et al., 2014, 2020).

Acknowledgments

This work was partially supported by the Deutsche Forschungsgemeinschaft (German Research Foundation) under project LU1174/8-1 (PACOG) of the research unit FOR1898, and under SPP 1788 (CoSIP) project CH1482/3-1 (CS-PMSE-MIMO).

Open Research Data Statement

PMSE radar spectra and imaging data as well as meteor wind data, can be found here `https://www.radar-service.eu/radar/en/dataset/RDOybenOQktKPLsT?token=MIPFqNPRJYOxNGsasNXi`. DNS data can be requested to the authors.

References

Adcock, T. A. A., & Taylor, P. H. (2014). The physics of anomalous ('rogue') ocean waves. *Reports on Progress in Physics*, *77*(10). doi: 10.1088/0034-4885/77/10/105901.

Berera, A., & Brener, D. J. (2020). On the force of vertical winds in the upper atmosphere. *Royal Society Open Science*, *submitted*. Retrieved from `http://arxiv.org/abs/2008.02884`.

Chau, J. L., Stober, G., Hall, C. M., Tsutsumi, M., Laskar, F. I., & Hoffmann, P. (2017). Polar mesospheric horizontal divergence and relative vorticity measurements using multiple specular meteor radars. *Radio Science*, *52*(7), 811–828. doi: 10.1002/2016RS006225.

Chau, J. L., Strelnikova, I., Schult, C., Oppenheim, M. M., Kelley, M. C., Stober, G., & Singer, W. (2014). Nonspecular meteor trails from non-field-aligned irregularities: Can they be explained by presence of charged meteor dust? *Geophysical Research Letters*, *41*(10), 3336–3343. doi: 10.1002/2014GL059922.

Chau, J. L., Urco, J. M., Avsarkisov, V., Vierinen, J. P., Latteck, R., Hall, C. M., & Tsutsumi, M. (2020). Four-Dimensional Quantification of Kelvin-Helmholtz Instabilities in the Polar Summer Mesosphere Using Volumetric Radar Imaging. *Geophysical Research Letters*, *47*(1), D09S12. doi: 10.1029/2019GL086081.

Dewan, E. M., & Picard, R. H. (2001). On the origin of mesospheric bores. *Journal of Geophysical Research Atmospheres*. doi: 10.1029/2000JD900697.

Ecklund, W. L., & Balsley, B. B. (1981). Long-term observations of the Arctic mesosphere with the MST radar at Poker Flat, Alaska. *J. Geophys. Res.*, *86*(7775-7780). doi: 10.1029/JA086iA09p07775.

Feraco, F., Marino, R., Pumir, A., Primavera, L., Mininni, P. D., Pouquet, A., & Rosenberg, D. (2018). Vertical drafts and mixing in stratified turbulence: Sharp transition with Froude number. *EPL*, *123*(4), 44002. doi: 10.1209/0295-5075/123/44002.

Fritts, D. C., Baumgarten, G., Wan, K., Werne, J., & Lund, T. (2014). Quantifying Kelvin-Helmholtz instability dynamics observed in noctilucent clouds: 2. Modeling and interpretation of observations. *Journal of Geophysical Research: Atmospheres*, *119*(15), 9359–9375. doi: 10.1002/2014JD021833.

Fritts, D. C., Kaifler, N., Kaifler, B., Geach, C., Kjellstrand, C. B., Williams, B. P., ... Wang, L. (2020). Mesospheric Bore Evolution and Instability Dynamics Observed in PMC Turbo Imaging and Rayleigh Lidar Profiling Over Northeastern Canada on 13 July 2018. *Journal of Geophysical Research: Atmospheres*. doi: 10.1029/2019JD032037.

Fritts, D. C., Williams, B. P., She, C. Y., Vance, J. D., Rapp, M., Lübken, F. J., ... Goldberg, R. A. (2004). Observations of extreme temperature and wind gradients near the summer mesopause during the MaCWAVE/MIDAS rocket campaign. *Geophysical Research Letters*. doi: 10.1029/2003GL019389.

Gardner, C. S., & Liu, A. Z. (2007). Seasonal variations of the vertical fluxes of heat and horizontal momentum in the mesopause region at Starfire Optical Range, New Mexico. *Journal of Geophysical Research Atmospheres*. doi: 10.1029/2005JD006179.

Gardner, C. S., Tao, X., & Papen, G. C. (1995). Simultaneous lidar observations of vertical wind, temperature, and density profiles in the upper mesophere: Evidence for nonseparability of atmospheric perturbation spectra. *Geophysical*

Research Letters. doi: 10.1029/95GL02783.

Gudadze, N., Stober, G., & Chau, J. L. (2019). Can VHF radars at polar latitudes measure mean vertical winds in the presence of PMSE?. *Atmospheric Chemistry and Physics*, *19*(7), 4485–4497. doi: 10.5194/acp-19-4485-2019.

Hoppe, U.-P., & Fritts, D. C. (1995). High-resolution measurements of vertical velocity with the European incoherent scatter VHF radar: 1. Motion field characteristics and measurement biases. *J. Geophys. Res.*, *100*(D8), 16813–16825. doi: 10.1029/95JD01466.

Hoppe, U.-P., Hall, C., & Röttger, J. (1988). First observations of summer polar mesospheric backscatter with a 224 MHz radar. *Geophysical Research Letters*, *15*(1), 28–31. doi: 10.1029/GL015i001p00028.

Hysell, D. L., & Chau, J. L. (2006). Optimal aperture synthesis radar imaging. *Radio Sci.*, *41*, RS2003. doi: 10.1029/2005RS003383.

Larsen, M. F., & Meriwether, J. W. (2012). Vertical winds in the thermosphere. *Journal of Geophysical Research: Space Physics*, *117*(9), A09319. doi: 10.1029/2012JA017843.

Latteck, R., Singer, W., Rapp, M., Vandepeer, B., Renkwitz, T., Zecha, M., & Stober, G. (2012). MAARSY: The new MST radar on Andøya – System description and first results. *Radio Sci.*, *47*(1), RS1006. doi: 10.1029/2011RS004775.

Laughman, B., Fritts, D. C., & Werne, J. (2009). Numerical simulation of bore generation and morphology in thermal and Doppler ducts. *Annales Geophysicae*, *27*(2), 511–523. doi: 10.5194/angeo-27-511-2009.

Lehmacher, G. A., Scott, T. D., Larsen, M. F., Bilén, S. G., Croskey, C. L., Mitchell, J. D., ... Collins, R. L. (2011). The Turbopause experiment: Atmospheric stability and turbulent structure spanning the turbopause altitude. *Annales Geophysicae*. doi: 10.5194/angeo-29-2327-2011.

Li, F., Swenson, G. R., Liu, A. Z., Taylor, M., & Zhao, Y. (2007). Investigation of a "wall" wave event. *Journal of Geophysical Research*, *112*(D4), D04104. doi: 10.1029/2006JD007213.

Lübken, F.-J., Jarvis, M. J., & Jones, G. O. L. (1999). First in situ temperature measurements at the Antarctic summer mesopause. *Geophysical Research Letters*, *26*(24), 3581–3584. doi: 10.1029/1999GL010719.

Marino, R., Mininni, P. D., Rosenberg, D. L., & Pouquet, A. (2014). Large-scale

anisotropy in stably stratified rotating flows. *Phys. Rev. E*, *90*(2), 23018. doi: 10.1103/PhysRevE.90.023018.

Marino, R., Rosenberg, D., Herbert, C., & Pouquet, A. (2015). Interplay of waves and eddies in rotating stratified turbulence and the link with kinetic-potential energy partition. *Europhysics Letters*, *112*(4). doi: 10.1209/0295-5075/112/49001.

Pouquet, A., Rosenberg, D., Marino, R., & Herbert, C. (2018). Scaling laws for mixing and dissipation in unforced rotating stratified turbulence. *Journal of Fluid Mechanics*, *844*, 519–545. doi: 10.1017/jfm.2018.192.

Rapp, M., & Lübken, F.-J. (2004). Polar mesosphere summer echoes ({PMSE}): {Review} of observations and current understanding. *Atmospheric Chemistry and Physics*, *4*, 2601–2633. doi: 10.5194/acp-4-2601-2004.

Sato, K., Kohma, M., Tsutsumi, M., & Sato, T. (2017). Frequency spectra and vertical profiles of wind fluctuations in the summer Antarctic mesosphere revealed by MST radar observations. *Journal of Geophysical Research: Atmospheres*, *122*(1), 3–19. doi: 10.1002/2016JD025834.

Smith, S. M., Stober, G., Jacobi, C., Chau, J. L., Gerding, M., Mlynczak, M. G., ... Umbriaco, G. (2017). Characterization of a Double Mesospheric Bore Over Europe. *Journal of Geophysical Research: Space Physics*, *122*(9), 9738–9750. doi: 10.1002/2017JA024225.

Taylor, M. J., Turnbull, D. N., & Lowe, R. P. (1995). Spectrometric and imaging measurements of a spectacular gravity wave event observed during the ALOHA-93 Campaign. *Geophysical Research Letters*, *22*(20), 2849–2852. doi: 10.1029/95GL02948.

Thomas, G. E., & Olivero, J. J. (1986). The heights of polar mesospheric clouds. *Geophysical Research Letters*, *13*(13), 1403–1406. doi: 10.1029/GL013i013p01403.

Tippett, M. K., & Cohen, J. E. (2016). Tornado outbreak variability follows Taylor's power law of fluctuation scaling and increases dramatically with severity. *Nature Communications*, *7*, 10668. doi: 10.1038/ncomms10668.

Urco, J. M., Chau, J. L., Weber, T., & Latteck, R. (2019). Enhancing the spatio-temporal features of polar mesosphere summer echoes using coherent MIMO and radar imaging at MAARSY. *Atmospheric Measurement Techniques*, *12*,

955–969. doi: 10.5194/amt-12-955-2019.

Von Zahn, U., Lübken, F. J., & Putz, C. (1990). BUGATTI experiments: mass spectrometric studies of lower thermosphere eddy mixing and turbulence. *Journal of Geophysical Research*, *95*(D6), 7443–7465. doi: 10.1029/JD095iD06p07443.

Widdel, H.-U. (1991). Experimental evidence for solitary waves in the middle atmosphere. *Journal of Geophysical Research: Space Physics*, *96*(A9), 15931–15942. doi: 10.1029/91ja01396.

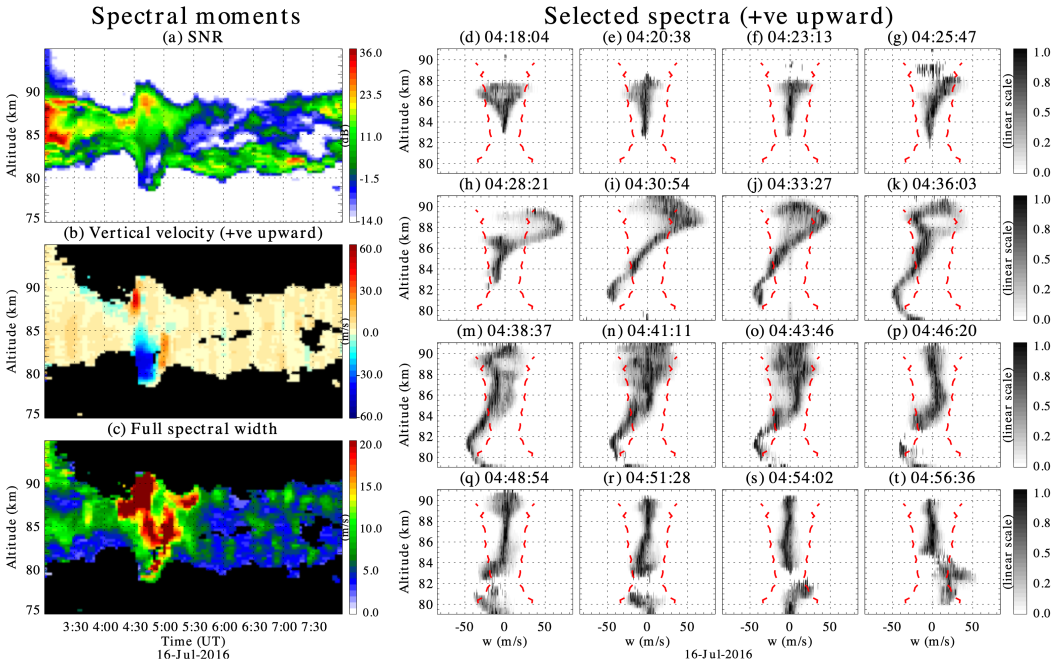

Figure 1. (Left) Range-time plots of: (a) signal-to-noise ratio (SNR), (b) vertical velocity (positive upward), and (c) total spectral width, observed with a vertical pointing beam on July 16, 2016. Note the relative large scales being shown for vertical velocities (± 60 ms^{-1}). (Right) Normalized spectra as a function of w, where $w = -f\lambda/2$, f is Doppler frequency in Hz, and λ the radar wavelength in meters. The normalization is in power spectra amplitude for each altitude with respect to its maximum. Three-sigma levels ($3\sigma_w$) based on June–July 2016 observations are plotted in dashed red lines.

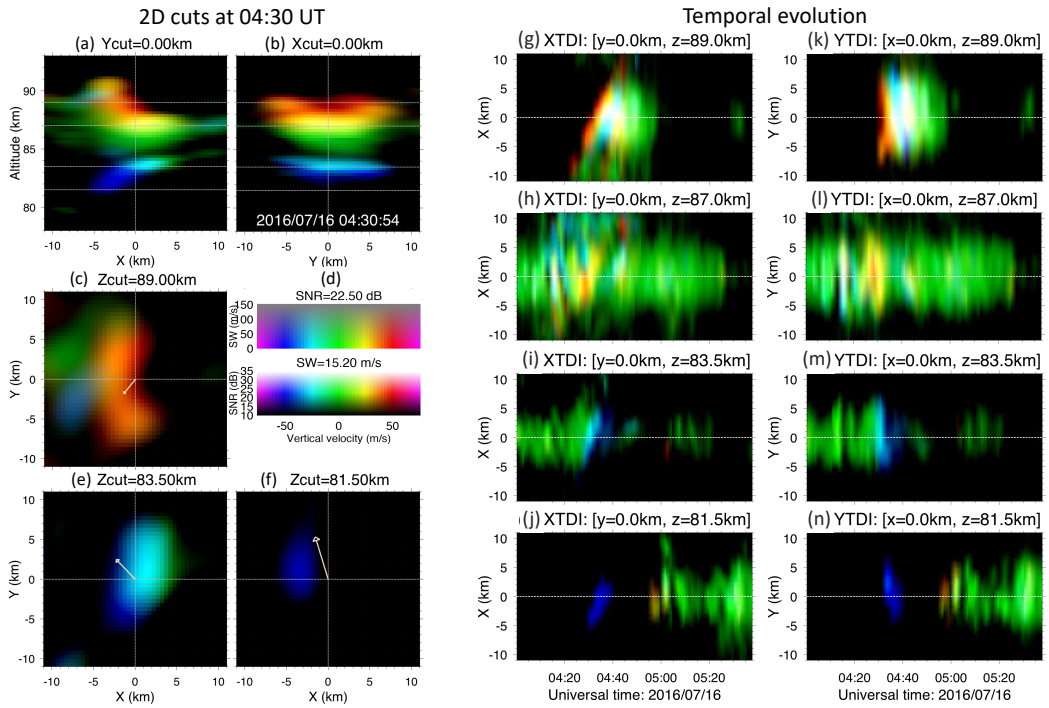

Figure 2. (Left) Two dimensional spatial cuts of PMSE inside the illuminated volume on July 16, 2016 around 0430 UT. xz and yz cuts at $x = 0$ and $y = 0$ km in panels (a) and (b), respectively. xy cuts at altitudes 89.0, 83.5, and 81.5 km in panels (c), (e), and (f), respectively. The intensity indicates signal strength of the echoes, while the color shows vertical velocity. Red (blue) values represent upward (downward) velocities greater (smaller) than 25 (-25) ms^{-1}, while green values represent velocities in between (see panel d). The 30-min horizontal wind from the specular meteor radar is indicated with a yellow arrow in the center of each xy cut. (Right) Space-time cuts at altitudes 89.0, 87.0, 83.5, and 81.5 km, of xy cuts in the left panel: (g-j) x versus time for $y = 0$, and (k-n) y versus time for $x = 0$.

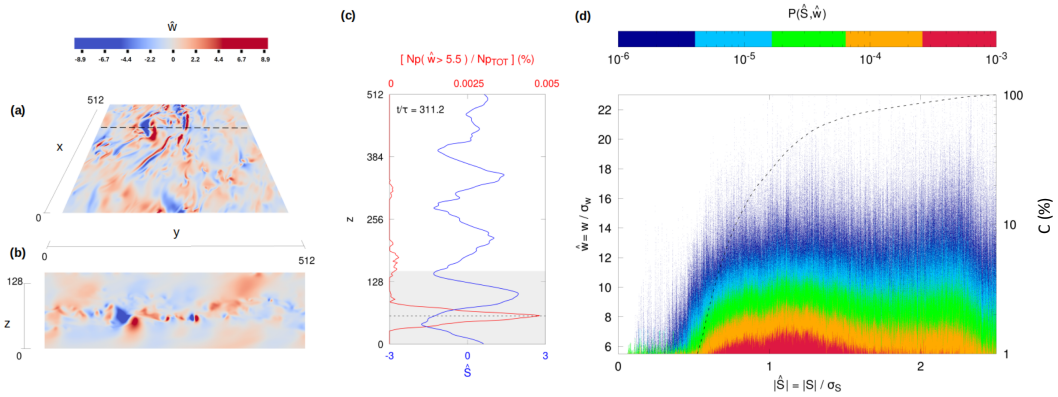

Figure 3. Two dimensional renderings of vertical velocity from the DNS: a) yx cut at fixed z and b) yz cut at fixed x, locations of cuts being indicated with dashed lines in panels a) and c). Panel c) shows the horizontal wind shear vertical profile $\hat{S} = S/\sigma_S$, together with the by-plane percentage of extreme events in the vertical velocity (defined as the grid points with $w > 5.5\sigma_w$). Panel d) reports the probability $P(\hat{w}, \hat{S})$ of observing extreme events in vertical velocity ($\hat{w} = w/\sigma_w$) conditioned to the values of the vertical shear of the horizontal wind velocity $\hat{S}$. Values larger than $\hat{S} = 2.5$ have been discarded as the statistics are not well resolved. The dashed line (panel d) represents the cumulative probability.

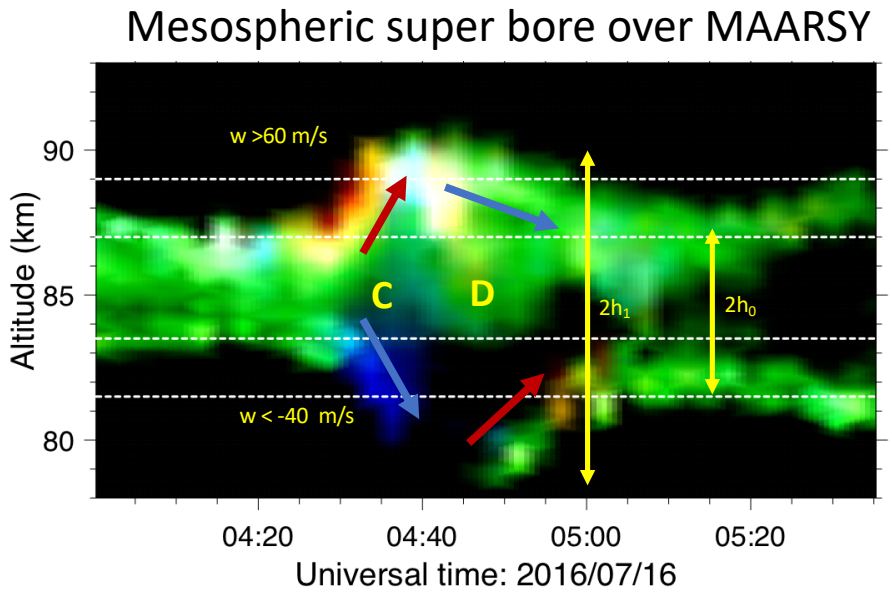

Figure 4. Closeup of the observations shown in Figure 1 to sketch the dynamics accompanying the bore. The color code is the same as the one in Figure 2d. The regions of strong updraft (downdraft) are indicated with red (blue) arrows. Letter C and D represent horizontal wind convergence and divergence, respectively. Yellow vertical arrows indicate relevant vertical scales (see text).